THE GEOLOGICAL SOCIETY OF AMERICA®

Subduction-zone contributions to axial volcanism in the Oman–U.A.E. ophiolite

Thomas M. Belgrano and Larryn W. Diamond
ROCK–WATER INTERACTION GROUP, INSTITUTE OF GEOLOGICAL SCIENCES, UNIVERSITY OF BERN, BALTZERSTRASSE 3, 3012 BERN, SWITZERLAND

ABSTRACT

Over four decades of research on the Semail ophiolite (Oman–U.A.E.) has greatly influenced our understanding of processes occurring at fast-spreading ocean ridges. While the well-developed sheeted dike complex and comagmatic lower pillow lavas indicate that the early Semail crust formed at a spreading axis, the precise tectonic setting of this axis—whether true mid-ocean ridge, back-arc or "proto"-arc—is contentious. This is largely because the tectonic implications of the geochemistry of the main axial volcanic unit (Geotimes/V1) are disputed. We bypass this hurdle by focusing on intercalations of primitive lavas that are depleted relative to mid-ocean-ridge basalt and that are deeply intercalated within the early Geotimes axial volcanostratigraphy throughout the northern ophiolite. Our analyses of these intercalations show a clear trace-element influence from a subducting slab. We interpret the depleted axial melts to have formed by localized, high-degree partial melting assisted by a high-Th/Nb slab fluid. These results confirm a deep subduction influence on the entire axial spreading phase of the world's largest ophiolite. Considered in the context of later hydrous and boninitic Alley volcanism and of insight from modern tectonic environments, our observations support a proto-arc, subduction-initiation setting for the origin of the Semail ophiolite.

LITHOSPHERE GSA Data Repository Item 2019137 https://doi.org/10.1130/L1045.1

INTRODUCTION

The Semail ophiolite (Oman–U.A.E; Fig. 1A) is often viewed as an archetypal analogue for modern, fast-spreading mid-ocean ridges (MOR). Although the vast sheeted dike complex (SDC) and comagmatic pillow lavas (known as the Geotimes or V1 unit; Fig. 1B) indicate that the early Semail crust formed at an axial spreading ridge, the validity of the MOR analogy remains controversial. The tectonic setting of axial spreading is the most fundamental issue of contention, with arguments primarily focusing on the relative timing of subduction initiation during the ophiolite's formation. The arguments are broadly divisible into support for the commencement of subduction prior to the axial spreading marked by Geotimes/V1 magmatism (e.g., Alabaster et al., 1982; Haase et al., 2016; Lippard et al., 1986; MacLeod et al., 2013; Pearce et al., 1981; Rioux et al., 2016; Rollinson and Adetunji, 2013) versus support for subduction initiation after spreading at a true MOR but before proto-arc Alley and Boninitic Alley (V2) magmatism (e.g., Einaudi et al., 2000; Ernewein et al., 1988; Godard et al., 2006; Kusano et al., 2014; Nicolas et al., 2000; Nicolas and Boudier, 2017; Umino et al., 1990). Resolution of this debate is essential to assign the correct tectonic setting to the axial processes recorded by the ophiolite, to constrain the relative timing between axial magmatism and subduction initiation, and to allow more detailed work on plate tectonic configurations to proceed.

A classic approach to identifying the tectonic setting of axial spreading in ophiolites is to analyze the immobile trace elements in their basal lavas and comagmatic SDC and compare these fingerprints to those of modern settings (Pearce, 2014). This approach has revealed a supra-subduction zone (SSZ) environment for spreading in many Tethyan ophiolites (e.g., Dilek and Furnes, 2009; Pearce et al., 1984). However, application of the same approach in the Semail ophiolite results in the basal (Geotimes) lava sequence and SDC being essentially indistinguishable from mid-ocean ridge basalt (MORB) (e.g., Einaudi, et al., 2003; Godard et al., 2006; Kusano et al., 2012; Miyashita et al., 2003). Slightly negative Nb–Ta anomalies and (fluid-mobile) Ba enrichment in Geotimes spilites are similar to some basalts collected from back-arc and fore-arc spreading settings (A'Shaikh et al., 2005; Pearce et al., 1981) and are thus supportive, but not definitively so, of a weak subduction zone influence. Further progress on this issue has been held back by the paucity of fresh Geotimes glasses, which in other ophiolites permit a more rigorous assessment of subduction-related enrichment of fluid-mobile elements. This inconclusive status has allowed the idea of a pre-subduction axial spreading phase in Oman to persist as an exception among Tethyan ophiolites.

Recent studies, however, have cast considerable doubt on the plausibility of a true MOR phase for the Semail ophiolite, as follows.

(1) Studying podiform mantle chromitites, Rollinson and Adetunji (2013, 2015) showed that a continuous series of melt compositions from MORB-like to boninitic are recorded by chromite compositions, concluding that such a series is best explained by the progressive transitions associated with subduction initiation settings.

(2) Investigating the plutonic sequence in the Haylayn and Semail blocks, both Koga et al. (2001) and Koepke et al. (2009) concluded that wehrlites in Oman formed from water-contaminated melts that were otherwise MORB-like in terms of incompatible element geochemistry. These observations imply that the water required for wehrlite petrogenesis

Thomas M. Belgrano http://orcid.org/0000-0003-2160-1895

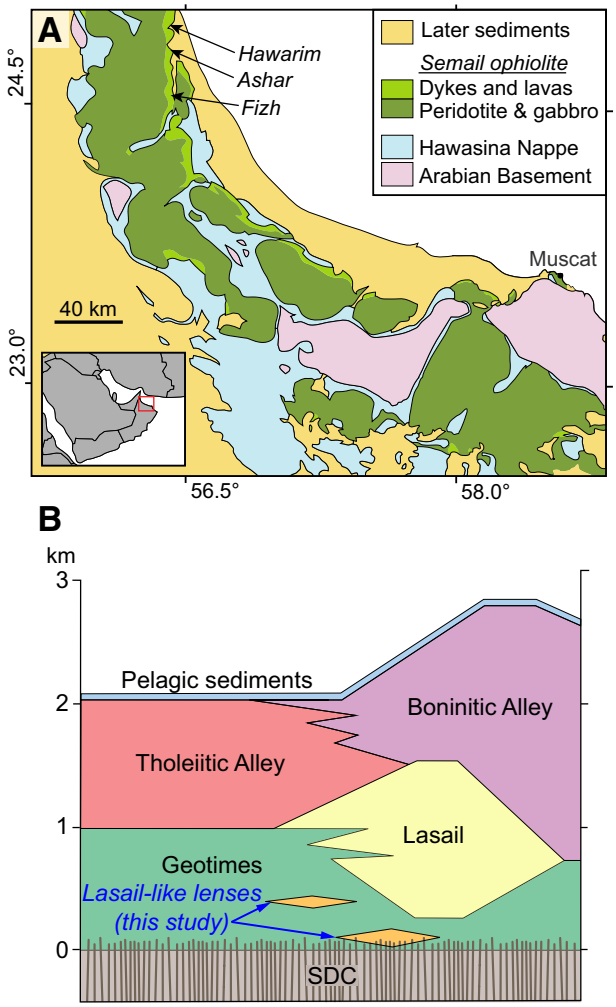

Figure 1. (A) Simplified geological map of the Hajar Mountains adapted from Calvez and Lescuyer (1991) and Gilgen et al. (2014) showing the Hawarim, Ashar, and Fizh volcanic section localities in the northern ophiolite. (B) Regional volcanostratigraphy of the Semail ophiolite modified after Alabaster et al. (1982) and Gilgen et al. (2014) with "Lasail-like lenses" documented in this study. SDC—sheeted dike complex.

(Koepke et al., 2009) may have been present during MORB-like axial phase magmatism.

(3) Haase et al. (2016) further documented plutons with Th/Nb ratios higher than in MORB and with ages apparently equivalent to axial intrusions between 96.40 ± 0.17 and 95.50 ± 0.17 Ma (Rioux et al., 2013). Other radiometric dates from diorite pods in the metamorphic sole (96.16 ± 0.022 Ma; Rioux et al., 2016) and from sediment-derived granites intruding the ophiolitic mantle (99.3 ± 3.3 Ma; Spencer et al., 2017) also overlap with the main phase of axial plutonism deduced by Rioux et al. (2013). Perhaps most significantly, Guilmette et al. (2018) recently used garnet Lu-Hf chronology to date prograde metamorphism at 103.2 ± 1.2 Ma and 104.1 ± 1.1 Ma at two metamorphic sole localities at either end of the ophiolite. Together, these radiometric constraints indicate that the Semail ophiolite was situated above a subduction zone at ca. 96 Ma.

(4) Focusing on the extrusive section, A'Shaikh et al. (2005) supported a back-arc basin setting for axial spreading based on similar arguments to Pearce et al. (1981), namely negative Nb-Ta anomalies and variable incompatible element depletion of the axial sequence. This geochemistry, however, has also been interpreted by some as contaminated MORB produced in a ridge-subduction setting similar to the Chile Ridge (e.g., Nicolas and Boudier, 2017; Sturm et al., 2000).

(5) Further evidence against a true mid-ocean ridge axial setting derives from differences in the major-element fractionation trends between Geotimes and MORB (MacLeod et al., 2013). Based on modeling these trends at different water contents, MacLeod et al. (2013) deduced that axial spreading was accompanied by hydrous input from a subducting slab along the length of the ophiolite. However, these deductions partly rely on elements susceptible to hydrothermal mobilization, which renders them suspect for some workers (e.g., Kusano et al., 2017), whereas others view the hydrous input as having been derived from deeply circulated seawater (e.g., Rospabé et al., 2017).

Considering the above body of evidence, it is perhaps surprising that the detailed chemostratigraphic studies available for the basal volcanic sequence (e.g., A'Shaikh et al., 2005; Einaudi et al., 2003; Godard et al., 2006; Kusano et al., 2012) have not revealed more conclusive arguments for subduction influence during axial magmatism. A generally overlooked, but potentially important line of evidence for this debate are the intercalations of pale Lasail-like lavas reported deep within the Geotimes axial sequence at several locations in the northern ophiolite (Alabaster et al., 1982; Umino et al., 1990). The Lasail unit typically overlies Geotimes as discontinuous, "seamount"-like accumulations of primitive basaltic lavas, but it may also interfinger and mix with the uppermost Geotimes lavas (Fig. 1B; A'Shaikh et al., 2005; Alabaster et al., 1982; Kusano et al., 2012; Umino et al., 1990). This stratigraphy has led to the general interpretation of Lasail as off-axis lavas that are mostly later than, and only locally coeval with the final stage of axial spreading (e.g., Kusano et al., 2012). The limited descriptions and geochemical analyses available for the deeply intercalated pale lavas are compatible with them being early Lasail unit basalts. However, due to their unusual stratigraphic position, these Lasail-like layers have either been dismissed as late sills or grouped with the Geotimes unit (Alabaster et al., 1982; Umino et al., 1990). As the Lasail unit has been interpreted to be arc-transitional (Alabaster et al., 1982), these early axial intercalations may record a more conclusive subduction signal than typical Geotimes.

In the following we confirm by field observations and geochemical analyses that these pale intercalations are closely comparable to normal Lasail lavas and that they erupted during earliest Geotimes axial volcanism. Crucially, we show that these early layers also contain contributions from a subducting slab. This finding confirms the growing evidence for a subduction influence during the entire Geotimes/V1 axial spreading phase. In light of this new constraint we discuss the feasibility of previously proposed tectonic settings for the axial phase of ophiolite formation, concluding that spreading in a proto-arc, subduction-initiation setting is the most viable scenario.

APPROACH

We first describe three examples of pale, primitive basalts that exhibit the field characteristics of the Lasail unit and that occur as discrete layers deep within the Geotimes axial unit. We refer to these pale intercalations from the outset as "Lasail-like" lenses in our figures and we go on to justify their affiliation to the widespread Lasail unit on geochemical grounds in the Discussion. These examples include a new occurrence in the Wadi Hawarim area of the Aswad block and two cases previously described along volcanic transects in Wadi Ashar (where we resampled after Alabaster et al., 1982) and in Wadi Fizh (Kusano et al., 2012) in the Fizh block (Fig. 1A). At the Hawarim and Ashar localities we mapped

these Lasail-like intercalations and sampled the enclosing axial strata, scrutinizing the outcrops and structures to ensure the sections are stratigraphically continuous. The dips of ferromanganoan sediments (umbers) and lava flows were used to calculate stratigraphic distances from the underlying, contiguous SDC. At the Wadi Fizh section we visited the outcrops and confirmed a similar interlayering of pale-gray pillow lavas within the typical Geotimes sequence; however, for this site we refer to the detailed map, section descriptions, and geochemical analyses documented by Kusano et al. (2012).

Once we have demonstrated that these pale intercalations are lavas that erupted during earliest Geotimes volcanism, we apply a geochemical fingerprinting approach based on that of Pearce (2014) that entails (1) testing that key trace elements have not been mobilized by post-eruptive hydrothermal alteration; (2) evaluating whether the layers are geochemically equivalent to the normal Lasail unit; (3) examining the immobile elements in standard diagrams that test for subduction influence; and (4) invoking petrogenetic arguments to explain the documented compositions and hence constrain the sources and mechanisms of melt generation.

ANALYTICAL METHODS

Igneous clinopyroxenes (cpx) in samples from each locality were measured using a Jeol™ JXA-8200 electron microprobe with a beam voltage of 20 kV, a beam current of 15 nA, and a spot size of 3 μm. The standards used were natural wollastonite (Si, Ca), albite (Na), and chrome spinel (Cr), and synthetic forsterite (Mg), anorthite (Al), tephrite (Mn), ilmenite (Fe, Ti), and bunsenite (Ni). Measurements of the standards run as unknowns are reported in Data Repository Table A7[1]. Analyses were accepted for use in this study only if the oxides of the analyzed elements summed to between 99 and 101 wt% and if the cations summed to between 3.97 and 4.03 moles when normalized to six moles of oxygen per formula unit.

Whole-rock major element compositions were determined on a PANalytical™ Axios wavelength-dispersive X-ray fluorescence (XRF) instrument with a rhodium source tube at voltages of 20–60 kV and beam currents of 40–100 mA according to the procedure described by Gilgen et al. (2014, 2016). For consistency with these studies, vanadium was also measured by XRF. All other trace-element concentrations were determined by laser-ablation–inductively coupled–plasma mass spectrometry (LA-ICP-MS) of ultra-finely milled, pressed-powder pellets at the University of Bern following exactly the procedure of Peters and Pettke (2016). For this, agate-milled rock powders were further wet-milled to an ultrafine powder, dried at 70 °C for ~5 h, and then combined with a cellulose binder and pressed into a pellet. The LA-ICP-MS measurements of these pellets were conducted on a GeoLas-Pro 193 nm ArF Excimer™ laser system in combination with an ELAN DRC-e™ quadrupole mass spectrometer. Basalt glass GSD-1G (U.S. Geological Survey; reference values from Jochum et al., 2005) was used as the primary calibration standard and all major elements were also analyzed, allowing the anhydrous trace-element concentrations to be calculated in the program SILLS (Guillong et al., 2008) by closure to 100 wt% oxides plus trace elements, with all Fe calculated as Fe_2O_3. The mean values of six ablations per sample are reported herein, with precision and pellet homogeneity indicated by one standard deviation (1σ) of the shots and propagated through the plotted element ratios. Accuracy was monitored through measurements of basalt standard BRP-1 (Cotta and Enzweiler, 2008) and highly depleted komatiite standard OKUM (Kane et al., 2007) prepared using an identical method to the samples, in addition to normal ablations of basalt glass BCR-2G (reference values from Jochum et al., 2005). Our measurements reproduce the standard values within 2.3% for all major elements, and within either 10% or the uncertainty on the reference value for all utilized trace elements except Ta, which was measured 10%–27% lower than the standard values. The limits of detection for each ablation, calculated in SILLS by the Pettke et al. (2012) method, are all significantly lower than the concentrations of analytes reported for our samples (see Tables A1–A7 in the Data Repository for full results, standard analyses, and limits of detection summary).

RESULTS

Volcanostratigraphic Sections

Wadi Hawarim

The Wadi Hawarim locality (Figs. 2A, 3A, and 4A) is situated in the Aswad block, the northernmost area of the Semail ophiolite with a fully exposed volcanic sequence. Despite tectonic disruption along N–S faults, the mapped volcanic section is continuous, and frequent umbers record a mean dip of 33° toward 163°SSE. At a stratigraphic distance of ~585 m above the SDC–Geotimes transition, a 20-cm-thick umber marks the beginning of an 85-m-thick layer of pillow lavas that have the appearance of the Lasail lava unit (marked in Figs. 3 and 4 as Lasail-like lenses). That is, they are pale grayish green, are composed of small bun-shaped pillows and pahoehoe flows, and have abundant white variolites in the flow rims (for a review of field characteristics, see Gilgen et al., 2014). This pale layer is traceable over 1200 m along strike. At the basal and top contacts, large, dark, hematitic Geotimes pillows are sharply juxtaposed against the small, pale-green pillows (Fig. 2A). The overlying Geotimes pillows interlock directly with pillows from the pale layer (thereby ruling out a faulted or intrusive contact) and continue upwards for a further 310–370 m (depending on where the section is taken) until terminating in a 1-m-thick umber overlain by massive flows of the Alley unit.

In thin section, the Geotimes lavas have a mostly intersertal texture, with abundant albitized plagioclase laths (30–50 vol%) and variably present euhedral clinopyroxenes (0–10 vol%). Particular to the Hawarim Geotimes lavas, and to the Aswad block in general, are common sub-equant, relatively fresh plagioclase phenocrysts. The interstices between plagioclase and clinopyroxenes are made up of Fe-Ti oxides (~5 vol%) and chlorite–epidote–quartz altered groundmass (the remainder). Relative to Geotimes, the Lasail-like lavas have a similar texture, made up of mostly albitized plagioclase laths (30–40 vol%) and a chlorite–epidote–quartz altered groundmass but with more abundant, coarser-grained clinopyroxenes (10–25 vol%), and less Fe-Ti oxides (1–5 vol%). This lack of Fe-Ti oxides explains the generally pale color of the Lasail-like lenses (Fig. 2).

Wadi Ashar

The Wadi Ashar section (Figs. 2B, 3B, and 4B) features several visually similar layers and pockets of Lasail-like lavas near the base of Geotimes, which were originally noted by Alabaster et al. (1982). The stratigraphy varies along strike, with the base of the largest pale intercalation lying just 15 m above the mapped SDC contact in the north (Fig. 3B). This layer is truncated to the north by a major strike-slip fault and thins from ~150 m to ~25 m true thickness in the south of the mapped area. The contact between pillow lavas and the SDC is transitional over some 100 m, and pockets of pale lavas 5–10 m in width exist across the mapped SDC contact whereas pockets of Geotimes pillows persist up to 40 m beneath the mapped SDC

[1]GSA Data Repository Item 2019137, Tables A1–A7, sample locations, results, standard analyses, and limits of detection, is available at http://www.geosociety.org/datarepository/2019, or on request from editing@geosociety.org.

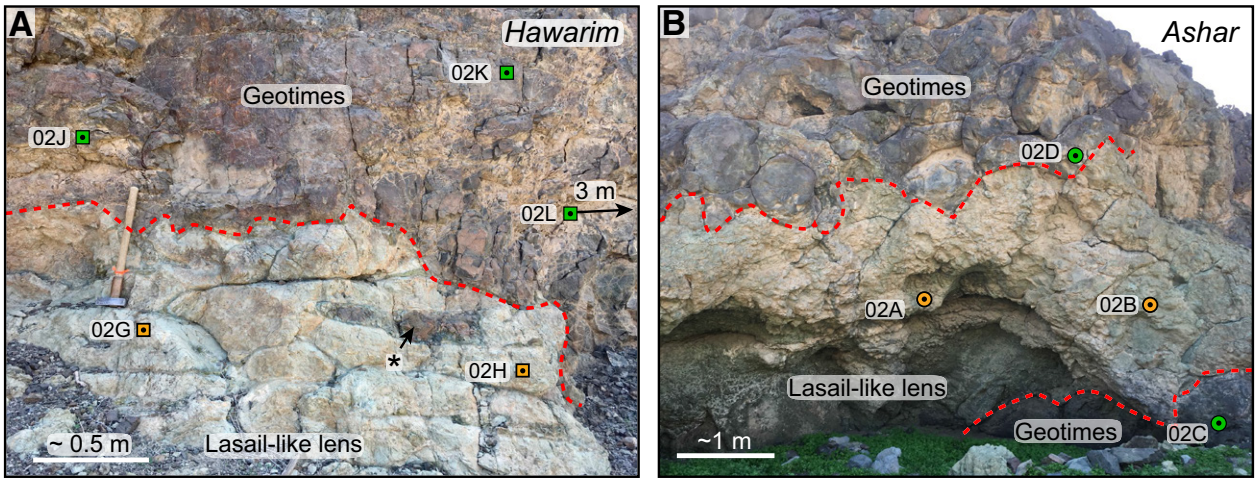

Figure 2. Pale gray-green Lasail-like lavas deeply intercalated within Geotimes lavas, showing sites sampled to assess element mobility (see text). (A) Pale Lasail-like pillow/pahoehoe flows underlying brown Geotimes pillows at the top of the Hawarim Lasail layer (lat/long: 24.8355°, 56.3174°). Asterisk: Geotimes-like pillow mixed into Lasail-like pillows. (B) Lens (~3 m thick) of pale, Lasail-like pillows between dark Geotimes pillows, ~10 m underneath the main Lasail-like layer at the Ashar locality (lat/long: 24.7519°, 56.3300°).

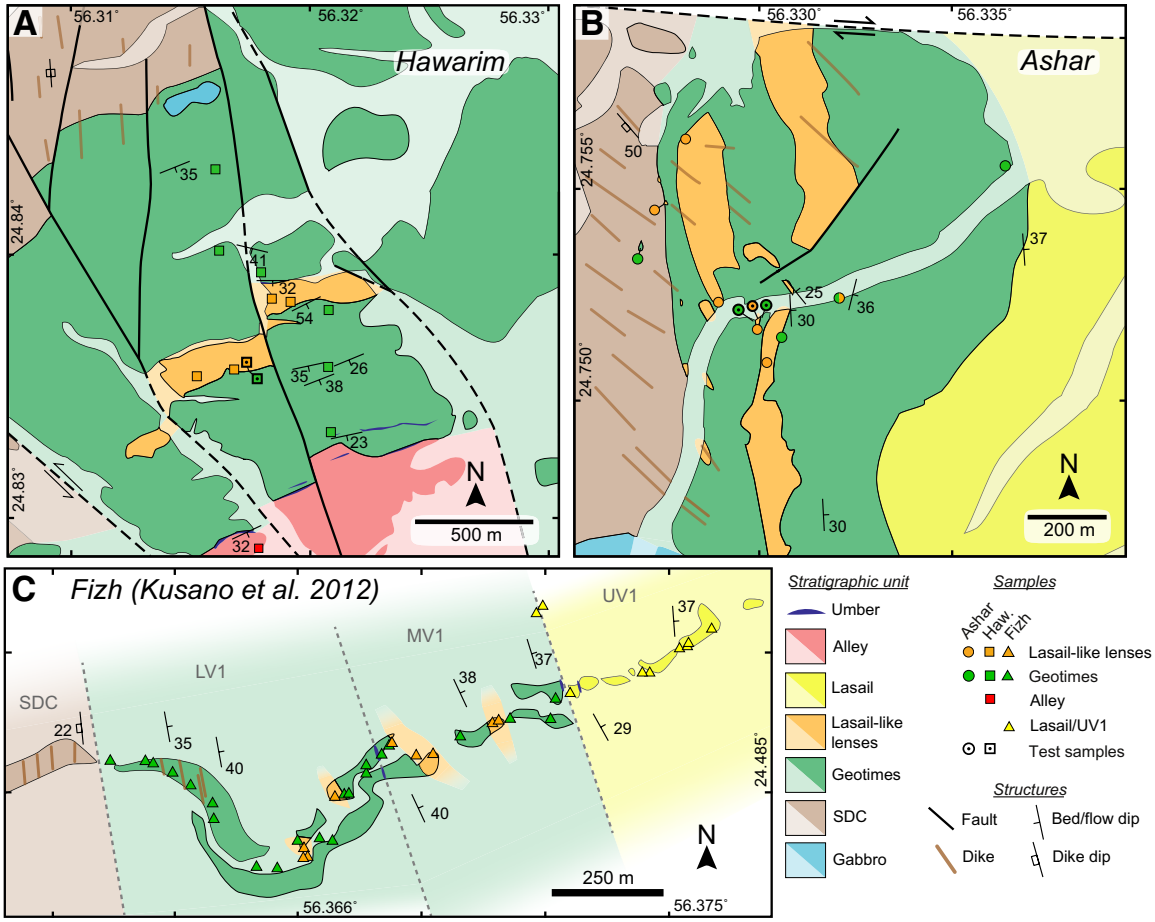

Figure 3. Geological field maps and sample locations of axial volcanics, showing Lasail-like lavas deeply intercalated within coeval Geotimes lavas. Coordinates refer to WGS84 grid. Dark-colored fields are outcrops, light-colored fields are inferred. Bold symbols with central dots: samples used to test element immobility (Fig. 2). (A) Wadi Hawarim map and samples (squares) remapped after BRGM (1993a). (B) Wadi Ashar map and samples (circles) remapped after BRGM (1993b). (C) Wadi Fizh map and samples (triangles) simplified after Kusano et al. (2012) showing unit boundaries including Lasail-like intercalations interpreted in this study. LV1, MV1, UV1: stratigraphic designations of Kusano et al. (2012) shown for reference. SDC—sheeted dike complex.

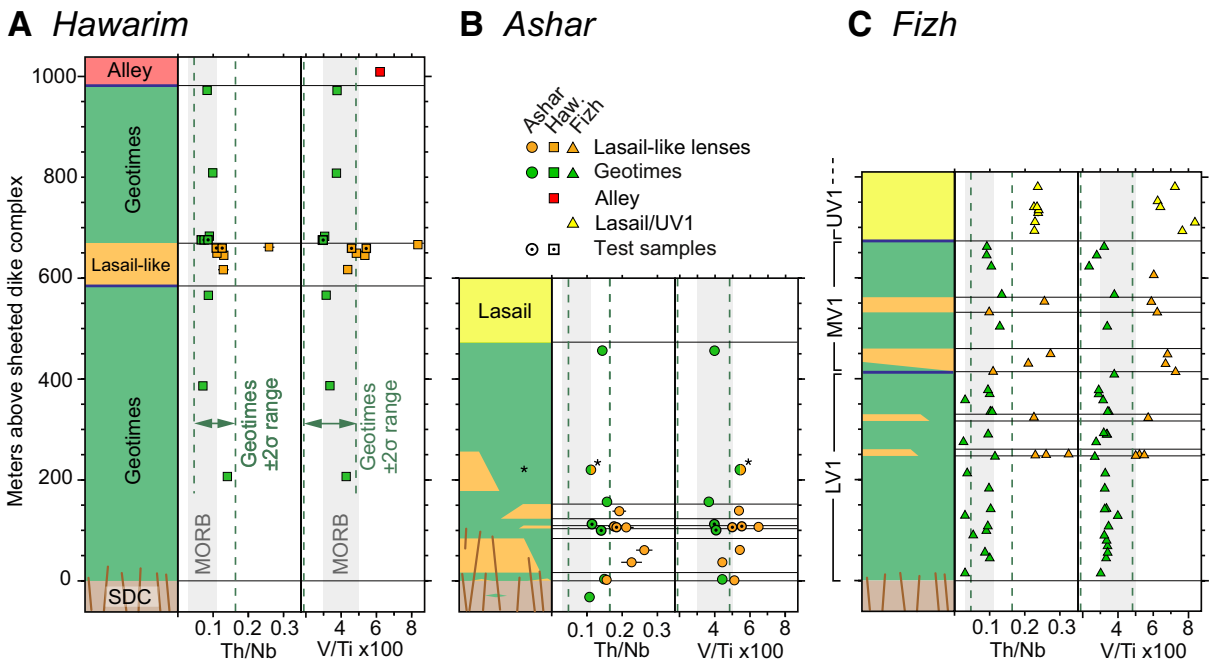

Figure 4. Volcanostratigraphic sections based on maps in Figure 3 correlated with whole-rock Th/Nb and V/Ti mass ratios. Samples are projected onto sections so as to preserve distance to the directly overlying contact. Error bars show propagated analytical precision (1σ) where larger than the symbol. (A) Hawarim with data in square symbols: this study. (B) Ashar with circles: this study. Asterisked sample taken from Geotimes-like lavas showing intermediate element ratios. (C) Fizh with boundaries of strata, LV1, MV1, UV1 designations and data (triangles) adapted from Kusano et al. (2012); depleted layers within LV1 and MV1 are identified in this study as Lasail-like layers (orange triangles); UV1 (yellow triangles) are interpreted as normal Lasail. Mid-ocean ridge basalt (MORB) fields (shaded) from Pearce (2008), Shervais (1982) and Geotimes unit mean ± 2σ (dashed) from compilation of Alabaster et al. (1982), Einaudi et al. (2000), Godard et al. (2003, 2006), Kusano et al. (2012, 2014, 2017), and Gilgen et al. (2014, 2016).

contact. Additional lenses of pale lavas a few tens of meters long and several meters thick (e.g., Fig. 2B) are common above and below the main layers. The overlying Geotimes section has a maximum thickness of ~400 m (including a second, laterally discontinuous 75-m-thick pale intercalation) before transitioning without an intervening umber into a thick sequence of normal Lasail unit lavas. The contacts between the pale intercalations and enveloping Geotimes lavas appear sharp in the field, with no umbers between the interlocking pillows of each unit (Fig. 2B). The mean dip of 31° toward 085°E is estimated from the mean of measurements of lava flows. Being so close to the SDC, the lowermost strata in the north of the mapping area are crosscut by abundant dikes that feed the overlying volcanic pile, demonstrating that no thrusting related to ophiolite emplacement has modified the volcanostratigraphy here (Fig. 3B).

In thin section, the Geotimes and Lasail-like lavas along the Ashar section are similar to those at Hawarim; however, sub-equant plagioclase phenocrysts are absent in the Ashar Geotimes lavas.

Wadi Fizh

Kusano et al. (2012) divided the Wadi Fizh axial volcanic sequence into lower, middle, and upper V1 (respectively LV1, MV1, UV1; Figs. 3C and 4C). Of these subdivisions, LV1 and MV1 were interpreted as equivalent to Geotimes, and UV1 as equivalent to Lasail. Moving up-section, visually and geochemically anomalous gray lava layers appear at around 250 m above the SDC and recur within the LV1 and MV1 sequence up to the UV1/Lasail contact (Figs. 3C, 4C; Kusano et al., 2012). The gray intercalations also display anomalous geochemistry (Fig. 3C), and we have differentiated them for comparison with the more typical Geotimes lavas along the Wadi Fizh section. As will be shown in the following, these anomalous layers are geochemically comparable to the pale Lasail-like intercalations documented at Hawarim and Ashar and are therefore considered together in the present study.

In thin section, Kusano et al. (2012) described a mixture of aphyric, hyalophitic, and intersertal textures with a similar mineralogy to the Ashar and Hawarim lavas, with the additional recognition of chlorite and clay pseudomorphs after olivine in many primitive samples.

Testing Trace-Element Immobility

The lavas at all three mapped sections are hydrothermally altered to lower-greenschist facies spilites, as described at similar stratigraphic levels throughout the ophiolite (Alabaster et al., 1982; Kusano et al., 2012; Lippard et al., 1986). A commonly utilized "window" through this alteration are relict magmatic clinopyroxenes, whose fresh compositions are generally preserved through spilite alteration (Fig. 5; Alabaster et al., 1982; Gilgen et al., 2014; Kusano et al., 2012). As far as the whole-rock is concerned, only hydrothermally immobile elements are reliable recorders of the original magmatic composition (Pearce, 2014). The whole-rock elements used in the present study (Ti, V, La, Nd, Sm, Yb, Nd, Cr, Y, Nb, Yb, Th, Ta, Zr, Hf) are widely considered to be immobile during this kind of alteration (e.g., Pearce, 1980, 2008). However, the standard tests described by Pearce (2014) cannot be readily applied to volcanic units which may be variably slab-influenced, or which may represent a range of mixtures between different magmas. An alternative test of hydrothermal immobility for this case was performed at the Hawarim and Ashar

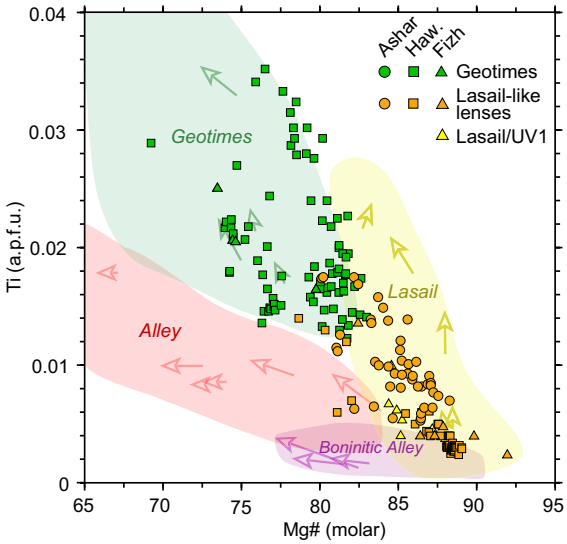

Figure 5. Clinopyroxene Ti content (atoms per formula unit) versus molar Mg# (= $Mg^{2+}/(Mg^{2+}+Fe^{2+})$) diagram to assess volcanostratigraphic affiliation, modified after Alabaster et al. (1982) and Gilgen et al. (2014, 2016). Symbols same as in Figure 4. Wadi Fizh depleted LV1/MV1 data from Kusano et al. (2012; yellow triangles) are recast as "Lasail-like" (this study). Semail unit fields from Alabaster et al. (1982), Gilgen et al. (2014, 2016), Ishikawa et al. (2002). Open arrows: core-to-rim trends of samples from each unit after Ishikawa et al. (2002) and Gilgen et al. (2014).

localities by analyzing nearby pillows from both the Lasail-like lenses and the contacting Geotimes lavas (Fig. 2). Here, we assume that the entire outcrop has undergone a similar style of alteration and that nearby pillows from within each unit originally had similar compositions upon eruption. If each stratigraphic unit is homogeneous in terms of subduction contributions and magma mixing history, then the ratios of immobile elements in samples from one unit should be consistent across the outcrop and they should contrast with those of the other unit. The samples analyzed to test for this consistency are highlighted (as bold symbols with central dots) for comparison throughout our figures.

In Figure 6A, although measurable differences exist in absolute Ti and V contents between samples from the same unit and outcrop, the element ratios are consistent enough to allow clear interpretation. In the $(La/Nd)_N$–$(Sm/Yb)_N$ diagram (Fig. 6B), the spread between adjacent samples in Sm/Yb is limited, but there is considerable spread in La/Nd for the Lasail-like lens pair at Ashar. This results from a difference in La (0.5 µg/g) between the two samples. While these samples do not significantly lie outside the broader data set, the variation in La may indicate limited local mobilization of this element. In the Th/Yb–Nb/Yb diagram (Fig. 7A), the samples from the same unit in each outcrop are generally consistent with each other within uncertainty, with the exception of one outlier with lower Th/Yb from the Hawarim Geotimes outcrop. Highly localized, minor hydrothermal mobilization of Th (e.g., causing an ~0.1 µg/g depletion) is a possible explanation, but this is not supported by any noticeable differences in mobile major elements between the samples. A more plausible explanation is that the sampled pillow had a slightly different magma mixing history with Geotimes, which is consistent with the observation of a small Geotimes-like pillow mixed into the Lasail-like layer in Figure 2A (asterisked). Despite these minor discrepancies, the excellent clustering of our results with published analyses of the same units supports the accuracy of our analyses and confirms the suitability of the utilized elements as hydrothermally immobile petrogenetic indicators. However, the variability in trace-element ratios within each lens suggests that they are internally heterogeneous.

Assessing Volcanostratigraphic Affiliation

To determine whether the deeply intercalated "Lasail-like" layers are petrologically related to the normal Lasail unit in its typical stratigraphic position, we have combined the whole-rock and cpx compositional fingerprints developed for unit identification by Alabaster et al. (1982), Godard et al. (2006) and Gilgen et al. (2014, 2016). Covariation of Mg# (molar Mg/(Mg+Fe) × 100) and Ti concentration in cpx is a reliable discriminant of the Semail units (Alabaster et al., 1982; Gilgen et al., 2014, 2016).

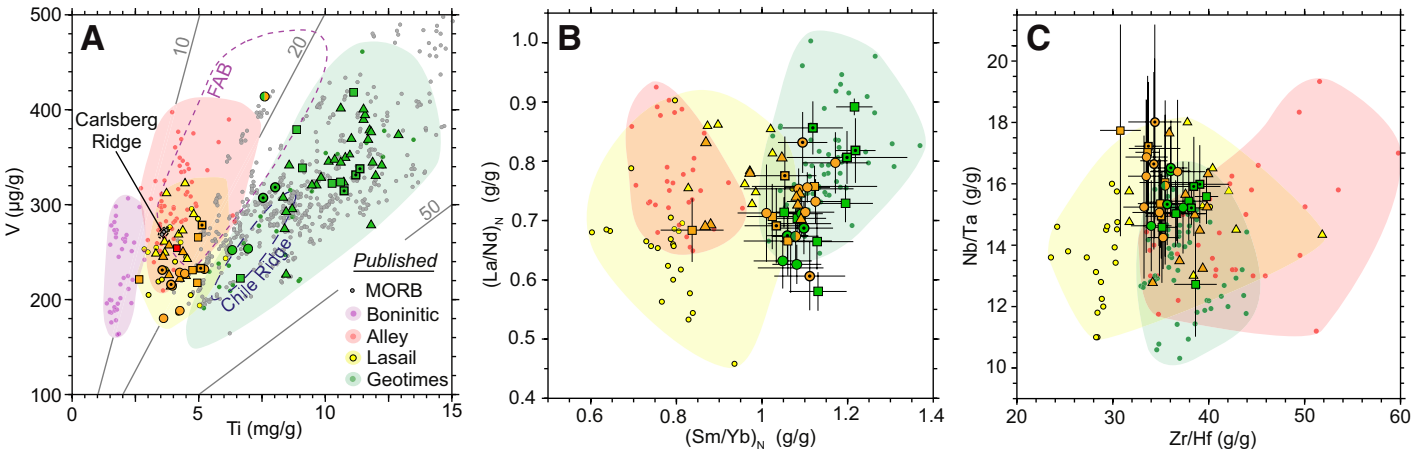

Figure 6. Whole-rock compositional diagrams to assess volcanostratigraphic affiliations. Symbols as in Figure 5. Shaded fields drawn around published analyses (sources given in Fig. 4). Error bars show propagated analytical precision (1σ) where larger than the symbol. (A) Ti–V plot after (Shervais, 1982) with Oman volcanic units. Gray lines: Ti/V ratios. IBM FAB: Izu-Bonin-Mariana fore-arc basalt field (Reagan et al., 2010; Ishizuka et al., 2011); Chile Ridge Contaminated mid-ocean ridge basalt (MORB) field: Karsten et al. (1996); MORB from Jenner and O'Neill (2012). (B) MORB-normalized La/Nd–Sm/Yb diagram (Godard et al., 2006). (C) Zr/Hf–Nb/Ta diagram (Godard et al., 2006), showing lack of discrimination between Alley and Lasail when recently collected Semail data are plotted.

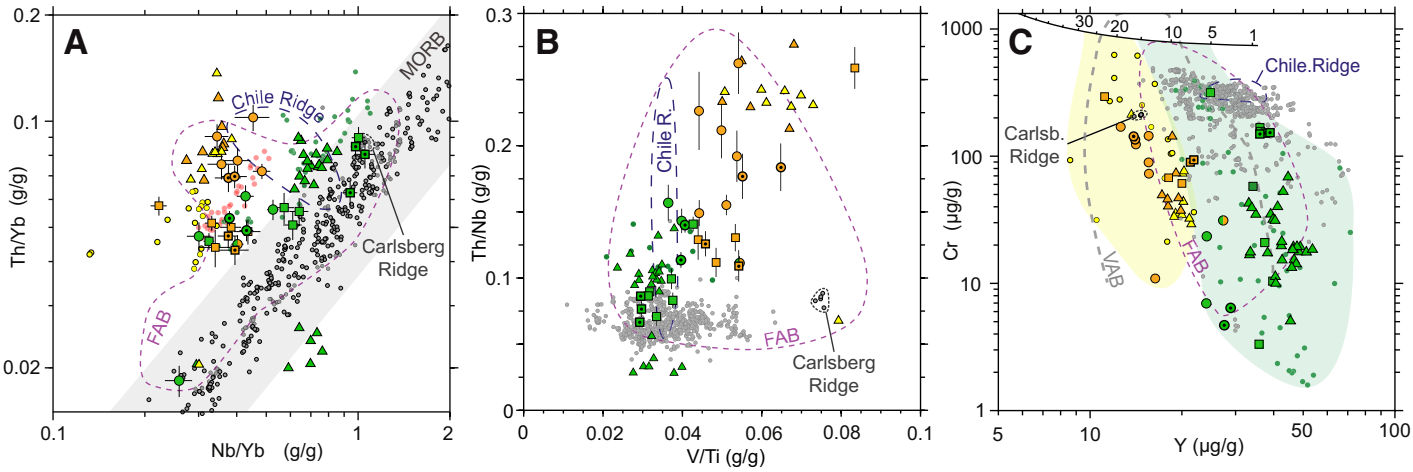

Figure 7. Diagrams to assess subduction influence. Symbols and field colors as in Figure 6. Error bars show propagated analytical precision (1σ) where larger than the symbol. (A) Th/Yb–Nb/Yb slab-influence diagram after Pearce (2008). Geotimes, Lasail, Alley fields: sources as in Figure 4. (B) Th/Nb–V/Ti diagram with mid-ocean ridge basalt (MORB) field defined by the key subduction-influence ratios of Pearce (2008) and Shervais (1982). (C) Cr–Y diagram with MORB and volcanic arc basalt (VAB) fields after Pearce (1980). Black graduated curve shows modeled batch melt compositions at increments (mass%) of partial melt of depleted MORB mantle (DMM), recalculated with Cr partition coefficients after Pearce (1980) and phase proportions; DMM composition and Y partition coefficients after Workman and Hart (2005). Sources of comparative data sets as in Figure 6A. FAB—fore-arc basalt field.

Figure 5 displays clinopyroxene analyses from a subset of samples from the Lasail-like intercalations and their enveloping Geotimes lavas at each locality, along with the unit compositional fields previously defined by Alabaster et al. (1982) and Gilgen et al. (2014, 2016). It is important to note that these fields are drawn around reported median and representative analyses, whereas all of our measured data are plotted in the figure to show the compositional variability at each locality. Clinopyroxene compositions from the Lasail-like intercalations are remarkably magnesian over a range of Ti values and cluster within the Lasail unit field. This contrasts with the lower Mg# of cpx from the Geotimes and Alley units (Mg# < 82.5) as well as with the generally stronger variation in Mg# with Ti content exhibited by the Alley units.

Whole-rock V–Ti compositions are used as a second discriminant of the units (Fig. 6A). Again, samples from the Lasail-like lenses generally fall within the Lasail unit field, at lower Ti and higher V/Ti ratios than Geotimes. One exception is a sample from the Ashar section, which has the field appearance of a Geotimes lava, but a V/Ti ratio intermediate with Lasail or Alley, consistent with other intermediate compositions previously reported from the area (Alabaster et al., 1982).

In addition to the above criteria, Godard et al. (2006) defined discriminatory fields between the Geotimes, Lasail and Alley units in a MORB-normalized La/Nd–Sm/Yb diagram and a Zr/Hf–Nb/Ta diagram (Figs. 6B and 6C). Since that study, however, further analyses have become available for Lasail and Alley (UV1 and LV2, respectively in Kusano et al., 2012, 2014), and their updated fields now have considerably more overlap. Nevertheless, the separation between Geotimes on the one hand and Lasail and Alley on the other remains visible along the Sm/Yb axis in Figure 6B. Here, unlike the bulk of the normal Lasail unit, the majority of analyses from the Lasail-like lenses plot along the Geotimes array.

Subduction Fingerprints

The V–Ti diagram (Shervais, 1982) has proved particularly effective at distinguishing volcanostratigraphic units in ophiolitic and fore-arc settings (Pearce, 2014; Reagan et al., 2010). This discrimination is based on the diagram's combined sensitivity to Ti depletion and the redox-dependent compatibility of V (Pearce, 2014). Elevated V/Ti relative to typical MORB can be explained by either elevated degrees of partial melting or oxidation of the mantle source, or by a combination of the two, which may occur when water is added to the source (Feig et al., 2006; Kelley and Cottrell, 2009; Mallmann and O'Neill, 2009; Shervais, 1982). Analyses of the Lasail-like lenses plot along a high V/Ti array in Figure 6A that overlaps with the Lasail, Alley, and fore-arc basalt fields but there is no overlap with analyses of the enveloping Geotimes lavas, which instead scatter across the MORB array. These elevated V/Ti ratios are clearly localized within the Lasail-like layers along the chemostratigraphic sections (Fig. 4).

Figure 7 shows analyses of the Lasail-like lavas and their enveloping Geotimes on three further diagrams designed to assess subduction influence. In the Th/Yb–Nb/Yb diagram (Fig. 7A), which assesses the input of a deeply derived, high Th/Nb subduction component (Pearce, 2008), the majority of Geotimes samples plot ambiguously along the upper boundary of the MORB array, with subordinate clusters at both lower and higher Th/Nb ratios. Contrastingly, analyses of the Lasail-like lenses overlap with neither the main Geotimes nor MORB arrays (see also Fig. 4). Instead these compositions overlap with the normal Lasail field, which encompasses a range of Th/Nb ratios elevated above the MORB array. In addition, analyses from the Lasail-like and normal Lasail lavas fall along a sub-vertical dispersion trend that runs discordantly to, and thus is inconsistent with MORB (Pearce, 2008).

Combining the diagnostic subduction-influence proxies of the Shervais (1982) and Pearce (2008) diagrams in the Th/Nb–V/Ti diagram allows the covariation of these two ratios to be assessed. In Figure 7B, the Geotimes samples spread along an array of compositions overlapping with but discordant to the MORB array, whereas analyses from both the Lasail-like lenses and Lasail in its normal stratigraphic positions plot well outside of the MORB array. When all the analyses from the Fizh, Ashar, and Hawarim sections are considered, the data do not divide clearly into units, but instead fall along a continuous, broadly correlated ($R^2 = 0.58$) array. This continuity shows that these element proxies for subduction influence are correlated and vary continuously between the two volcanic units.

The Cr–Y diagram (Fig. 7C) compares the concentration of a highly compatible element (Cr) with an incompatible element (Y). This permits

assessment of incompatible element depletion, partial melting systematics, and fractionation paths (Pearce, 1980). Analyses of the Lasail-like lenses fall along a fractionation trend at lower Y for a given Cr concentration relative to Geotimes. Moreover, it is clear from these trends that the two lava suites neither converge at high Cr nor lie along a common fractionation path.

MORB-normalized incompatible element trends for the Lasail-like lenses generally overlap with the range of compositions defined by the normal Lasail unit (Fig. 8A). However, as also expressed by Sm/Yb (Fig. 6B), the slope between the light and medium rare-earth elements is slightly flatter for the Lasail-like lenses than for Lasail in its normal stratigraphic position. In comparison to MORB, SW Indian Ridge MORB, and Chile Ridge MORB, the Lasail-like lenses exhibit an overall depletion of trace elements with pronounced negative Nb and positive Th anomalies (Figs. 8A–8C). This Th enrichment is sufficient for Th_N/La_N ratios to be at or above unity. In comparison to the "depleted V1" (~Lasail) primary melt composition calculated by the addition of 6 wt% olivine to a depleted V1 composition from Wadi Fizh (Kusano et al., 2017), lavas from the Lasail-like lenses have similar compositions, though are marked by higher Th/Nb ratios. One Lasail-like lens sample from Wadi Hawarim (TB3-04B) is markedly more depleted than typical Lasail lavas and is actually boninitic in terms of major elements (SiO_2 = 54 wt%, MgO = 9 wt%, TiO_2 = 0.44 wt%, V/Ti = 0.083), though these Si and Mg values may not be reliable owing to alteration.

The incompatible element trends of the Geotimes lavas along the documented sections overlap with those previously published for Geotimes, but also include several more depleted examples, which are intermediate with respect to Lasail and tend toward stronger negative Nb anomalies than typical Geotimes (Fig. 8A). In comparison to the "less-depleted V1" primary melt composition calculated by Kusano et al. (2017), which has a Th–Nb depleted, SW Indian MORB-like character (Fig. 8B), the majority of Geotimes analyses from the Ashar and Hawarim sections are enriched in Th and light rare-earth elements over Nb.

DISCUSSION

Lasail-Like Intercalations

Timing and Occurrence with Respect to Axial Volcanism

The maps and stratigraphic sections in Figures 3 and 4 document the intercalation of lenses of Lasail-like lavas deep within coeval Geotimes lavas at three localities in the northern ophiolite. The thick accumulations of Geotimes above these pale layers show that axial magmatism continued well after their eruption. In the Wadi Ashar section, the coincidence of the lowermost Lasail-like layers with the SDC–Geotimes contact, and its dissection by dikes emanating from the SDC, demonstrates unequivocally that these layers were erupted during the earliest stages of axial volcanism recorded in the northern ophiolite. Although these layers are only confirmed geochemically within the documented sections, similar intercalations between Lasail-like lavas and Geotimes have been reported from the Ghayth area of the SE Fizh block (A'Shaikh et al., 2005; Umino et al., 1990) and Wadi Mahmum in the Haylayn block (Umino et al., 1990). Apparently similar low-Ti, elevated Th/Nb intervals are also present deep within Geotimes as far south as Wadi Shaffan in the Sarami block (Einaudi et al., 2000, 2003). These layers are thus a recurrent feature at least throughout the northern ophiolite.

Magmatic Relationship with Respect to Typical Lasail

The pale intercalations at Ashar were initially described as Lasail lavas, but then attributed to a pulse of primitive magma from a Geotimes magma chamber (Alabaster et al., 1982). Similar occurrences of pale axial intercalations were described by Umino et al. (1990) as Lasail lavas and then grouped into "V1" on the basis of stratigraphy.

Our analyses indicate that, although they are clearly part of the axial sequence, the pale lavas along the Ashar and Hawarim sections are more similar to the normal Lasail unit than to their enveloping Geotimes lavas.

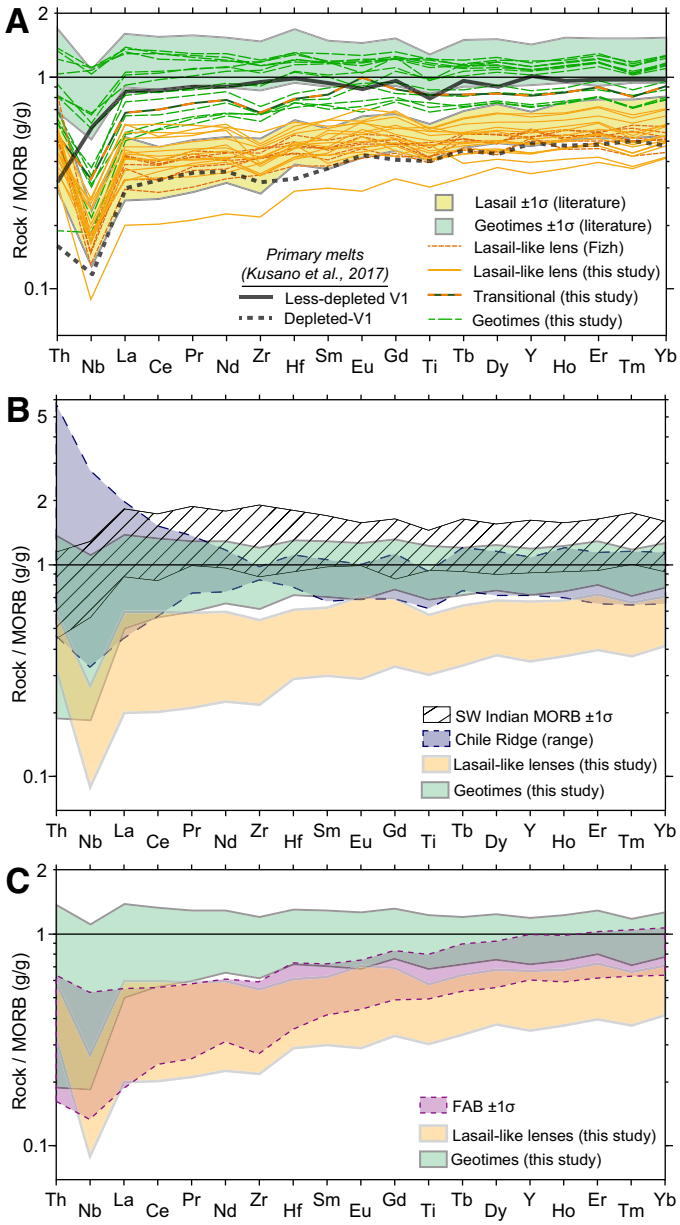

Figure 8. Whole-rock incompatible elements normalized to N-MORB (normal mid-ocean ridge basalt; Gale et al., 2013). (A) Curves show Lasail-like and enveloping Geotimes lavas from Hawarim and Ashar (this study), and Lasail-like/depleted-V1 data from Fizh (Kusano et al., 2012). Primary melt compositions for "Less-depleted V1" and "Depleted-V1" calculated by Kusano et al. (2017) for comparison with Geotimes and Lasail-like respectively. Shaded fields show mean ± 1σ from literature sources given in Figure 4. (B) Comparison of Geotimes and "Lasail-like" unit ranges from this study with SW Indian MORB (hachure shows mean ± 1σ; Coogan et al., 2004) and Chile Ridge C-MORB (contaminated mid-ocean ridge basalt) range (Karsten et al. 1996). (C) Data ranges of Geotimes and Lasail-like units from this study compared with Izu-Bonin-Mariana fore-arc basalts (FAB, mean ± 1σ; Ishizuka et al., 2011; Reagan et al., 2010).

This is supported by their identical field characteristics, similar incompatible element depletion at a given Cr content, high V/Ti ratios, and highly magnesian cpx compositions. In contrast to the normal Lasail lavas further up in the stratigraphy, these layers have, on average, slightly less compatibility-dependent depletion, which is expressed by their predominantly Geotimes-like Sm/Yb ratios and flatter incompatible element trends (Figs. 6B, 8A). According to our criteria, the depleted LV1 and MV1 layers along Wadi Fizh are also geochemically equivalent to the Lasail-like lenses at Ashar and Hawarim (Figs. 4–6).

The incompatible-element depletion and high V/Ti ratios of the Lasail-like lenses and Lasail in its normal stratigraphic position can both be explained by 20%–30% partial melting of the same depleted MORB mantle source that produced Geotimes (Godard et al., 2006; Shervais, 1982). The distinctly primitive nature of both the Lasail-like lenses and the normal Lasail basalts can be explained by limited fractionation from Mg- and Ca-rich parental melts produced by high-degree melting of a MORB source (Klein and Langmuir, 1987). This model may also explain the distinctly high-Mg# compositional field of the Lasail cpx (Fig. 5; Alabaster et al., 1982; Gilgen et al., 2014), as cpx should saturate earlier, and therefore at higher Mg# in high-Ca parental melts. However, the Mg# of the first cpx to crystallize from tholeiitic melts also increases with melt water content and pressure (Feig et al., 2006), so the origin of these compositions remains unclear.

Another potential explanation for the differences in incompatible element depletion among the Semail axial lavas could be preexisting mantle heterogeneities resulting from an earlier episode of localized melt extraction, as suggested for the Troodos ophiolite (Woelki et al., 2018; Regelous et al., 2014). Application of this model to the Semail axial suite would imply that the depleted Lasail-like layers were derived from the previously depleted mantle domains, whereas Geotimes was derived from the less-depleted domains. Klein and Langmuir (1987), however, noted that the solidus of such depleted domains should occur at higher temperatures than less-depleted mantle, and therefore that, all other factors being equal, the resultant primary melts should be of a lower degree and more evolved. The high-Cr contents and cpx Mg# of the Lasail-like layers rather indicate a particularly primitive parental melt (Figs. 5, 7C), and together with the elevated V/Ti better fit a model of primarily melt degree-controlled depletion.

We therefore interpret the Lasail-like intercalations to have formed in a similar way to that interpreted for the normal Lasail unit, namely by elevated degrees of partial melting of a source similar to Geotimes. The higher Sm/Yb ratios suggest that the axial, Lasail-like lenses may have originated from a slightly less-depleted source than the later off-axis Lasail phase. Alternatively, the Lasail-like axial lavas could represent mixtures of depleted Lasail melts mixed with a small proportion of less-depleted Geotimes melts. In any case, a range of different depletions, Sm/Yb and V/Ti ratios also exist for published analyses of the Lasail unit in its normal stratigraphic position (Figs. 5–7). In this context, the lenses fit as an early expression of the Lasail unit. In recognition of the mappable nature, wide geographic distribution and distinct geochemical signature of the lenses, we consider them to constitute a volcanic sub-unit of the axial sequence. We therefore refer to this subunit as "Axial Lasail" in the remainder of this manuscript.

Magmatic Relationship with Respect to Geotimes

When compared to Geotimes, analyses of the Axial Lasail lavas fall along contrasting arrays in the V/Ti diagram, and their fractionation paths are separate on the Cr-Y diagram (Figs. 6A and 7C). These differences do not necessarily preclude the derivation of the two units from a similar source (Godard et al., 2006). However, in the documented cases, they do preclude their derivation from a common parental melt (e.g., Alabaster et al. 1982; Lippard et al., 1986). This conclusion is supported by the contrasting parental melt compositions calculated for the "less-depleted V1" and "depleted V1" lavas by Kusano et al. (2017), which are essentially equivalent to Geotimes and Lasail, respectively (Fig. 8). Grouping Geotimes and Axial Lasail together on the basis of a shared source is therefore an oversimplification that fails to capture the key differences in melt production at the Semail spreading ridge.

Transitional compositions between Geotimes and Lasail are, however, present along the documented sections and are readily apparent in Figures 6–8. This range in compositions could be produced by varying partial melt degrees for a similar source, or alternatively, variable mixing ratios between depleted and less-depleted melts. Comparable transitional compositions have previously been reported at numerous locations across the northern ophiolite (Alabaster et al., 1982; Kusano et al., 2012; A'Shaikh et al., 2005).

Evidence for Subduction-Zone Influence

Having established that early expressions of Lasail-like volcanism occurred throughout the axial spreading-ridge phase recorded in the northern ophiolite, the key question as to whether this axial magmatism was contaminated by a subduction component may now be investigated through the geochemistry of these lavas.

Although we use Figure 6A principally to compare volcanostratigraphic units within the ophiolite, the V–Ti diagram can also provide information on tectonic setting (Shervais, 1982). However, this information is complicated by the petrogenetic ambiguity of elevated V/Ti ratios, which may be due to increased degrees of partial melt and/or oxidation of the mantle source (Mallmann and O'Neill, 2009; Shervais, 1982). Oxidation of the mantle source or melt is a strong indicator of supra-subduction zone melting in the presence of added water (Kelley and Cottrell, 2009). Higher degrees of partial melting are also typical but not diagnostic of supra-subduction settings (Pearce, 2014; Godard et al., 2006). As shown by Shervais (1982), the majority of MORB analyses plot along a low V/Ti array. This normal MORB array overlaps with Geotimes (Fig. 6A) but lies at lower V/Ti than the Axial Lasail layers. Assuming a similar source composition, this difference indicates that the parental melts of Axial Lasail formed by higher degrees of partial melting as well as possibly under more oxidized conditions than Geotimes or normal MORB.

Ratios of Th/Nb higher than MORB within the Axial Lasail lenses (Figs. 4, 7A) indicate that a deeply derived, Th-bearing, Nb-deficient slab component contaminated the source or parental melts of these lavas (Pearce, 2008). However, as the Lasail-like lenses are far more depleted than Geotimes, they are also more sensitive recorders of slab-additions in terms of Th/Nb (Pearce, 2008). These anomalous layers thus may not necessarily be more contaminated than many of the less-depleted, moderately elevated-Th/Nb Geotimes lavas along the documented sections (Figs. 7A, 8A). Nevertheless, comparison with the less-depleted V1 (Geotimes) primary melt composition calculated by Kusano et al. (2017) as well as several rather depleted but low Th/Nb analyses from Fizh and Hawarim (Fig. 7A) demonstrates that not all Geotimes lavas are similarly slab-contaminated. Addition of a deep slab component to the Semail mantle source was therefore apparently heterogeneous.

In arc lavas, enrichments in Th are generally attributed to additions of slab melts, as allanite-hosted Th is insoluble at temperatures below the solidus of subducted sediments (Hermann and Rubatto, 2009; Pearce, 2008). On the other hand, addition of a slab-derived aqueous fluid to the Alley (LV2) unit—which also has elevated Th/Nb (Fig. 7A)—has been argued on the basis of its similar Hf and Nd isotopic geochemistry with

Geotimes (Kusano et al., 2017), which is also similar to normal Lasail (Godard et al., 2006). This could be interpreted to indicate that the slab component added to the axial sequence was well mixed into the source that produced Geotimes, Lasail and Alley, such that all these melts are similarly isotopically-shifted. Considering the variability in Th/Nb just for Geotimes (Figs. 7A, 8A), this scenario seems implausible. Alternatively, the slab component could have been isotopically similar to the mantle source, such that no major isotopic shifts occurred during addition. The characteristics of the slab component required for axial contamination (both high Th/Nb and εNd = 7–10; Kusano et al., 2017) is therefore inconsistent with the sediment-derived melts and fluids thus far identified in Oman by Haase et al. (2015) and Ishikawa et al. (2005). A slab component derived from dehydration or melting of subducted, altered oceanic crust, as explored by Rollinson (2015), may better fit these constraints.

In the Cr–Y diagram (Fig. 7C), the Lasail unit falls within the volcanic arc basalt (VAB) trend, following a contrasting fractionation path to both Geotimes and the majority of MORB. During fractional crystallization, Cr is extracted from the melt by olivine, clinopyroxene, and Cr-spinel (Pearce, 1980). For dry MORB, the early onset of plagioclase fractionation (in which both Cr and Y are incompatible) passively enriches Y in the melt at relatively high-Cr contents (Pearce, 1980). Combined with its characteristically limited compositional range, this results in a relatively compact MORB Cr–Y field (Pearce, 1980). In wet SSZ melts, however, plagioclase crystallization is suppressed such that it may crystallize after cpx (in which Cr is compatible; Feig et al., 2006). The result is that wet SSZ melts follow a steeper path to lower Cr concentrations before changing slope toward higher Y at the onset of plagioclase fractionation (Pearce, 1980). The generally steeper and deeper path of both the Lasail and Geotimes suites in the Cr–Y diagram are therefore supportive of the elevated water contents and cpx-before-plagioclase crystallization order inferred for axial magmatism by MacLeod et al. (2013). The batch-melting curve plotted in Figure 7C is calculated based on approximated Cr partition coefficients and on the assumption of a depleted MORB mantle (DMM) source (Pearce, 1980; Workman and Hart, 2005). Accordingly, the intersection of each unit's extrapolated trend with the melting curve does not necessarily yield the exact extent of partial melting but does illustrate that the Axial Lasail lavas were either formed by higher degrees of partial melting, or from a more depleted source than MORB, both of which are typical features of SSZ lavas (Pearce, 1980).

Ruling Out Alternatives to SSZ Melting

Several alternative models have been proposed to explain the subduction-related geochemical signatures of the Semail ophiolite within the context of a true MOR setting. Although each model may explain certain features, we argue that none of them can account for both the hydrous, high-degree melting and high Th/Nb signatures of the Axial Lasail lavas.

Incompatible-element trends in the Lasail unit have previously been explained by mixing depleted, high-degree partial melts of DMM with small fractions of low-degree DMM melts in a MOR setting (Godard et al., 2006). Although Godard et al. (2006) demonstrated that the overall depletion of Lasail lavas can be explained by ~20% partial melting of DMM, their modeled mixtures of the high-degree melts with low-degree melts do not reproduce the elevated Th/Nb anomalies in the Axial Lasail lavas.

Similar high-degree or two-stage melting may explain depleted MORB outliers from the Carlsberg Ridge with elevated V/Ti and Y depletion similar to the Axial Lasail basalts (Figs. 6A, 7C). However, these anomalous Carlsberg Ridge basalts lack the negative Nb anomalies of the Lasail-like axial lavas, and instead plot coherently within the MORB array in Figures 7A and B.

Contaminated (C-)MORB erupting along spreading ridges at ridge-trench intersections (e.g., Chile Ridge) has Th/Nb ratios scattered higher than MORB and thus could arguably be compared to the Semail axial basalts and invoked to challenge their SSZ origin (e.g., Karsten et al., 1996; Moores et al., 2000; Nicolas and Boudier, 2017; Sturm et al., 2000). These signatures have been attributed to contamination of the mantle source by material derived through a window in the nearby down-going slab (Karsten et al., 1996; Moores et al., 2000). Metcalf and Shervais (2008) contested this scenario for axial basalts in many ophiolites, showing that the subduction signatures in the C-MORB examples are generally weaker than in ophiolites and, crucially, lack evidence for hydrous melting and fractionation. These arguments also apply to the Semail axial lavas (MacLeod et al., 2013; Metcalf and Shervais, 2008) and are supported by our data. For example, the Chile Ridge lavas have elevated Th/Nb ratios (Fig. 7A) but lack the high V/Ti ratios (Fig. 6A) and steep Cr–Y trend (Fig. 7C) that result from involvement of hydrous fluids during fractionation. The combination of these features is typical of SSZ basalts but absent in C-MORB settings (Metcalf and Shervais, 2008; Reagan et al., 2010). Moreover, Figure 8B shows that the elevated Th/Nb ratios in the Chile Ridge basalts are part of an overall enrichment in incompatible elements relative to MORB. This is common to other examples of C-MORB (e.g., Juan de Fuca and Woodlark ridges; Metcalf and Shervais, 2008) and starkly contrasts with the depleted Axial Lasail compositions.

An Indian Ocean mantle source heterogeneously modified by ancient, pre-Cretaceous subduction has also been invoked to explain the negative Nb anomalies and scattered Hf–Nd isotopic character of the Geotimes suite (Godard et al., 2006), which are similar to some SW Indian ridge basalts (e.g., Coogan et al., 2004). This scenario could feasibly explain the negative Nb anomalies within Geotimes along the sampled sections. However, the SW Indian ridge MORB anomalies are far subtler than those of the Axial Lasail lavas (Fig. 8B) and, again, this scenario does not explain the primitive nature of the Lasail-like lavas nor their hydrous melting signatures, nor those of Geotimes (MacLeod et al., 2013).

Deep infiltration of seawater and stoping of hydrothermally altered rocks into magma chambers have been suggested as alternative explanations for these hydrous melting signatures (Benoit et al., 1999; Boudier et al., 2000). However, MacLeod et al. (2013) pointed out the absence of any significant hydrous signatures in MORB fractionation trends that could be related to this process. Moreover, experimental hydrous melts generated by melting hydrothermally altered basalts at comparable conditions do not fractionate Th from Nb and are less, not more magnesian than their starting material, in stark contrast to the Axial Lasail lavas (France et al., 2014).

It is conceivable that ancient source modification, high-degree melting, and seawater infiltration operated in tandem to produce the observed set of subduction signals in a MOR setting, but in this case, their geochemical signatures should be independent of one another. Figure 7B demonstrates that this is not the case. The Carlsberg, Chile Ridge, and other MORB lava suites fall along either vertical or horizontal trends, whereas Th/Nb and V/Ti are correlated for Semail axial lava suite (Fig. 7B).

The consistent geochemical differences between the Lasail-like layers and anomalous MORB examples strongly favors a subduction-related origin for the Lasail-like axial layers, where high-degree partial melting of the axial mantle source was triggered by the addition of a water-bearing, high Th/Nb subduction component.

The Case for a Subduction Initiation Setting

The arguments above rule out an early, subduction-unrelated MOR phase for the Semail ophiolite, but do not clearly distinguish between

back-arc (A'Shaikh et al., 2005; Pearce et al., 1981) and proto-arc subduction-initiation models of ophiolite formation (Dilek and Furnes, 2009; MacLeod et al., 2013; Rollinson and Adetunji, 2013; Rollinson, 2015). However, the progressive source depletion and increase in subduction input recorded by the transition from MORB-like basalts (Geotimes) through "island arc"-tholeiites (Alley) to boninites (Boninitic Alley) in Oman (Fig. 1; Kusano et al., 2017; Rollinson and Adetunji, 2013) is remarkably similar to the evolution of the Izu-Bonin-Mariana (IBM) fore-arc prior to the establishment of steady subduction (Figs. 1, 7A, 8C; Dilek and Furnes, 2009; Ishizuka et al., 2011; MacLeod et al., 2013; Reagan et al., 2013; Shervais et al., 2018; Stern et al., 2012; Whattam and Stern, 2011). For example, primitive fore-arc basalts ("P-FAB") have recently been described atop the axial crust in the IBM fore-arc sequence in an identical stratigraphic position to the normal Lasail lavas in Oman (Shervais et al., 2018). Moreover, the duration of the magmatic evolution from basaltic to boninitic volcanism in the Semail ophiolite is remarkably similar to that of the IBM (ca. 2 Ma; Ishizuka et al., 2011; Reagan et al., 2019; Rioux et al., 2013).

The high temperatures inferred for both slab- and mantle-melting in the Semail ophiolite based on the presence of boninitic melts are also a typical feature of subduction initiation settings (Ishikawa et al., 2002; Rollinson, 2015). However, the reliability of boninites as indicators of proto-arc settings may be questioned following the observation of modern boninites in the Lau basin (Resing et al., 2011) and Tonga arc (Cooper et al., 2010). Though both settings are SSZ, neither is associated with ongoing subduction initiation. This leaves open the possibility of a back-arc genesis for the Semail ophiolite (A'Shaikh et al., 2005; Pearce et al., 1981), where the axial crust would have formed at a back-arc ridge and subsequently migrated to an arc or fore-arc position. A major problem with this interpretation is the short period allowed for this migration by the Semail geochronology (1–2 Ma; Rioux et al., 2013) as well as the continuous transition from Geotimes to Lasail volcanism documented herein. Finally, no coeval arc edifices exist in the Semail realm attesting to an arc-trench system mature enough to drive the back-arc spreading and subduction erosion rates required by such a model (Pearce et al., 1984; MacLeod et al., 2013).

Based on the above reasoning, we present in Figure 9 a simple model to illustrate a tectonic setting for ophiolite formation, which explains the documented slab-contributions to axial volcanism. This proto-arc–spreading model is based on that of Whattam and Stern (2011) and is broadly consistent with previously proposed models for Oman and other Tethyan ophiolites formed at a similar time and with similar volcanostratigraphies (Guilmette et al., 2018; Dilek and Furnes, 2009; Dilek et al., 2008; Dilek and Flower, 2003; MacLeod et al., 2013; Metcalf and Shervais, 2008; Rollinson and Adetunji, 2013; Stern et al., 2012).

One key difference between the Semail and IBM sequences are the MORB-like V/Ti ratios of the Geotimes unit versus the arc-like V/Ti ratios of the IBM axial fore-arc basalts. The pre-axial episode of melt extraction recently deduced for the IBM, but so far not for the Semail ophiolite, may explain this discrepancy (Shervais et al., 2018; Yogodzinski et al., 2018). However, slightly lower V/Ti fore-arc basalts have been found in the trench-distal IBM proto-arc crust sampled in the Amami-Sankaku basin (Hickey-Vargas et al., 2018). Somewhat comparable, Geotimes-like lava suites also exist in the Mirdita and Pindos ophiolites, and there have similarly been ascribed to a trench-distal, but nevertheless subduction-related setting (Dilek and Furnes, 2009; Dilek et al., 2008). Accordingly, though comparisons between the Semail and IBM sequences may be restricted by their apparently differing modes of subduction initiation (forced versus spontaneous, respectively; Guilmette et al., 2018; Arculus et al., 2015), the Semail axial crust appears to have formed in a supra-subduction zone setting distal to the trench and above relatively normal depleted-MORB mantle (Godard et al., 2006).

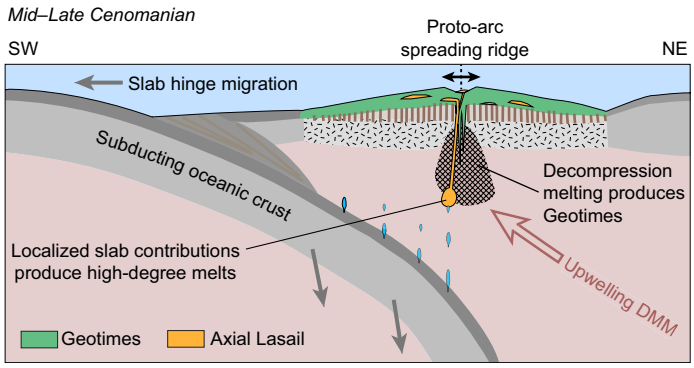

Figure 9. Conceptual diagram of the genesis of the Semail axial ophiolitic crust at ca. 96 Ma, including Geotimes and Axial Lasail units in a proto-arc–spreading setting. Subduction initiation had apparently commenced ~8 m.y. before this stage (Guilmette et al., 2018).

CONCLUSIONS

We have presented and reinterpreted the axial volcanostratigraphy at three localities in the northern Semail ophiolite. Our argument that the axial spreading phase of the Semail ophiolite occurred above a subduction zone rests on (1) the map evidence that Axial Lasail lavas were locally erupted throughout the Geotimes volcanic phase, (2) the clear slab-influenced geochemical signature of those lavas, and (3) the fact that the Geotimes unit and SDC are comagmatic and thus record axial magmatism (Alabaster et al., 1982; Umino et al., 1990). The above evidence directly confirms the input of deeply derived slab components to axial magmatism, placing the entire axial phase of ophiolite formation above a subduction zone.

These findings confirm the volcanostratigraphy originally presented by Alabaster et al. (1982), with Lasail layers deeply intercalated within Geotimes (Fig. 1). They further confirm the considerable body of independent evidence for SSZ axial spreading, which compels reassessment of published comparisons of the ophiolite to true MOR settings. When these results are considered in the context of previous work on the ophiolite as well as on modern analogues, the most viable tectonic scenario is that the Semail ophiolite began to form in a proto-arc setting during the early stages of subduction. Thus, the Semail outcrops constitute a uniquely detailed record of magmatism related to subduction initiation and they serve as a valuable and accessible counterpart to ongoing research on submarine fore-arcs.

ACKNOWLEDGMENTS

We thank Samuel Weber for field assistance; Daniel Peters, Thomas Pettke, and Oscar Laurent for help with LA-ICP-MS; Elias Kempf and Thomas Bovay for help with microprobe measurements; and Lydia Zehnda for the XRF measurements. We gratefully acknowledge the logistical support of Khalid al-Tobi (Earth Secrets Co., Oman), Salim Omar Al-Ibraheem, Mohammed Al Araimi, and Mohammed Al-Battashi (Public Authority for Mining, Sultanate of Oman). We kindly thank Peter Tollan and the reviewers of an earlier version of this manuscript, as well as two anonymous reviewers, whose comments greatly improved the present contribution, together with the editorial handling of Laurent Godin. This project was funded by Swiss National Science Foundation (SNSF) Grant 200020-169653 to L.W.D.

REFERENCES CITED

A'Shaikh, D., Miyashita, S., and Matsueda, H., 2005, The petrological and geochemical characteristics of an ophiolite volcanic suite from the Ghayth area of Oman: Journal of Mineralogical and Petrological Sciences, v. 100, p. 202–220, https://doi.org/10.2465/jmps.100.202.

Alabaster, T., Pearce, J.A., and Malpas, J., 1982, The volcanic stratigraphy and petrogenesis of the Oman ophiolite complex: Contributions to Mineralogy and Petrology, v. 81, p. 168–183, https://doi.org/10.1007/BF00371294.

Arculus, R.J., Ishizuka, O., Bogus, K.A., Gurnis, M., Hickey-Vargas, R., Aljahdali, M.H., Bandini-Maeder, A.N., Barth, A.P., Brandl, P.A., Drab, L., do Monte Guerra, R., Hamada, M., Jiang, F., Kanayama, K., et al., 2015, A record of spontaneous subduction initiation in the Izu–Bonin–Mariana arc: Nature Geoscience, v. 8, p. 728, https://doi.org/10.1038/ngeo2515.

Benoit, M., Ceuleneer, G., and Polvé, M., 1999, The remelting of hydrothermally altered peridotite at mid-ocean ridges by intruding mantle diapirs: Nature, v. 402, p. 514–518, https://doi.org/10.1038/990073.

Boudier, F., Godard, M., and Armbruster, C., 2000, Significance of gabbronorite occurrence in the crustal section of the Semail ophiolite: Marine Geophysical Researches, v. 21, p. 307–326, https://doi.org/10.1023/A:1026726232402.

BRGM (Bureau de Recherches Géologique et Minères), 1993a, Geological Map of Aswad: Ministry of Petroleum and Minerals, Sultanate of Oman, scale 1:50,000, sheet NG40-14B1/B2.

BRGM (Bureau de Recherches Géologique et Minères), 1993b, Geological Map of Fizh: Ministry of Petroleum and Minerals, Sultanate of Oman, scale 1:50,000, sheet NG40-14B4.

Calvez, J.-Y., and Lescuyer, J.L., 1991, Lead isotope geochemistry of various sulphide deposits from the Oman mountains, *in* Peters, T.J., et al., eds., Ophiolite Genesis and Evolution of the Oceanic Lithosphere, Proceedings of the Ophiolite Conference, Muscat, Oman, 7–18 January 1990, v. 5, p. 385–397, https://doi.org/10.1007/978-94-011-3358-6_19.

Coogan, L.A., Thompson, G.M., MacLeod, C.J., Dick, H.J.B., Edwards, S.J., Hosford Scheirer, A., and Barry, T.L., 2004, A combined basalt and peridotite perspective on 14 million years of melt generation at the Atlantis Bank segment of the Southwest Indian Ridge: evidence for temporal changes in mantle dynamics?: Chemical Geology, v. 207, p. 13–30, https://doi.org/10.1016/j.chemgeo.2004.01.016.

Cooper, L.B., Plank, T., Arculus, R.J., Hauri, E.H., Hall, P.S., and Parman, S.W., 2010, High-Ca boninites from the active Tonga Arc: Journal of Geophysical Research. Solid Earth, v. 115, https://doi.org/10.1029/2009JB006367.

Cotta, A.J.B., and Enzweiler, J., 2008, Certificate of Analysis of the Reference Material BRP-1 (Basalt Ribeirão Preto): Geostandards and Geoanalytical Research, v. 32, p. 231–235, https://doi.org/10.1111/j.1751-908X.2008.00894.x.

Dilek, Y., and Flower, M.F.J., 2003, Arc-trench rollback and forearc accretion: 2. A model template for ophiolites in Albania, Cyprus, and Oman, *in* Dilek, Y., and Robinson, P.T., eds., Ophiolites in Earth History: Geological Society of London Special Publication 218, p. 43–68, https://doi.org/10.1144/GSL.SP.2003.218.01.04.

Dilek, Y., and Furnes, H., 2009, Structure and geochemistry of Tethyan ophiolites and their petrogenesis in subduction rollback systems: Lithos, v. 113, p. 1–20, https://doi.org/10.1016/j.lithos.2009.04.022.

Dilek, Y., Furnes, H., and Shallo, M., 2008, Geochemistry of the Jurassic Mirdita Ophiolite (Albania) and the MORB to SSZ evolution of a marginal basin oceanic crust: Lithos, v. 100, p. 174–209, https://doi.org/10.1016/j.lithos.2007.06.026.

Einaudi, F., Pezard, P.A., Cochemé, J.-J., Coulon, C., Laverne, C., and Godard, M., 2000, Petrography, geochemistry and physical properties of a continuous extrusive section from the Sarami Massif, Semail Ophiolite: Marine Geophysical Researches, v. 21, p. 387–408, https://doi.org/10.1023/A:1026752415989.

Einaudi, F., Godard, M., Pezard, P., Cochemé, J.J., Coulon, C., Brewer, T., and Harvey, P., 2003, Magmatic cycles and formation of the upper oceanic crust at spreading centers: Geochemical study of a continuous extrusive section in the Oman ophiolite: Geochemistry Geophysics Geosystems, v. 4, https://doi.org/10.1029/2002GC000362.

Ernewein, M., Pflumio, C., and Whitechurch, H., 1988, The death of an accretion zone as evidenced by the magmatic history of the Sumail ophiolite (Oman): Tectonophysics, v. 151, p. 247–274, https://doi.org/10.1016/0040-1951(88)90248-X.

Feig, S.T., Koepke, J., and Snow, J.E., 2006, Effect of water on tholeiitic basalt phase equilibria: An experimental study under oxidizing conditions: Contributions to Mineralogy and Petrology, v. 152, p. 611–638, https://doi.org/10.1007/s00410-006-0123-2.

France, L., Koepke, J., MacLeod, C.J., Ildefonse, B., Godard, M., and Deloule, E., 2014, Contamination of MORB by anatexis of magma chamber roof rocks: Constraints from a geochemical study of experimental melts and associated residues: Lithos, v. 202–203, p. 120–137, https://doi.org/10.1016/j.lithos.2014.05.018.

Gale, A., Dalton, C.A., Langmuir, C.H., Su, Y., and Schilling, J.-G., 2013, The mean composition of ocean ridge basalts: Geochemistry Geophysics Geosystems, v. 14, p. 489–518, https://doi.org/10.1029/2012GC004334.

Gilgen, S.A., Diamond, L.W., Mercolli, I., Al-Tobi, K., Maidment, D.W., Close, R., and Al-Towaya, A., 2014, Volcanostratigraphic Controls on the Occurrence of Massive Sulfide Deposits in the Semail Ophiolite, Oman: Economic Geology and the Bulletin of the Society of Economic Geologists, v. 109, p. 1585–1610, https://doi.org/10.2113/econgeo.109.6.1585.

Gilgen, S.A., Diamond, L.W., and Mercolli, I., 2016, Sub-seafloor epidosite alteration: Timing, depth and stratigraphic distribution in the Semail ophiolite, Oman: Lithos, v. 260, p. 191–210, https://doi.org/10.1016/j.lithos.2016.05.014.

Godard, M., Dautria, J.M., and Perrin, M., 2003, Geochemical variability of the Oman ophiolite lavas: Relationship with spatial distribution and paleomagnetic directions: Geochemistry Geophysics Geosystems, v. 4, https://doi.org/10.1029/2002GC000452.

Godard, M., Bosch, D., and Einaudi, F., 2006, A MORB source for low-Ti magmatism in the Semail ophiolite: Chemical Geology, v. 234, p. 58–78, https://doi.org/10.1016/j.chemgeo.2006.04.005.

Guillong, M., Meier, D.L., Allan, M.M., Heinrich, C.A., and Yardley, B.W.D., 2008, Appendix A6: SILLS: A MATLAB-based program for the reduction of laser ablation ICP-MS data of homogeneous materials and inclusions: Mineralogical Association of Canada Short Course, v. 40, p. 328–333.

Guilmette, C., Smit, M.A., van Hinsbergen, D.J.J., Gürer, D., Corfu, F., Charette, B., Maffione, M., Rabeau, O., and Savard, D., 2018, Forced subduction initiation recorded in the sole and crust of the Semail Ophiolite of Oman: Nature Geoscience, v. 11, p. 688–695, https://doi.org/10.1038/s41561-018-0209-2.

Haase, K.M., Freund, S., Koepke, J., Hauff, F., and Erdmann, M., 2015, Melts of sediments in the mantle wedge of the Oman ophiolite: Geology, v. 43, p. 275–278, https://doi.org/10.1130/G36451.1.

Haase, K.M., Freund, S., Beier, C., Koepke, J., Erdmann, M., and Hauff, F., 2016, Constraints on the magmatic evolution of the oceanic crust from plagiogranite intrusions in the Oman ophiolite: Contributions to Mineralogy and Petrology, v. 171, p. 1–16, https://doi.org/10.1007/s00410-016-1261-9.

Hermann, J., and Rubatto, D., 2009, Accessory phase control on the trace element signature of sediment melts in subduction zones: Chemical Geology, v. 265, p. 512–526, https://doi.org/10.1016/j.chemgeo.2009.05.018.

Hickey-Vargas, R., Yogodzinski, G.M., Ishizuka, O., McCarthy, A., Bizimis, M., Kusano, Y., Savov, I.P., and Arculus, R., 2018, Origin of depleted basalts during subduction initiation and early development of the Izu-Bonin-Mariana island arc: Evidence from IODP expedition 351 site U1438, Amami-Sankaku basin: Geochimica et Cosmochimica Acta, v. 229, p. 85–111, https://doi.org/10.1016/j.gca.2018.03.007.

Ishikawa, T., Nagaishi, K., and Umino, S., 2002, Boninitic volcanism in the Oman ophiolite: Implications for thermal condition during transition from spreading ridge to arc: Geology, v. 30, p. 899–902, https://doi.org/10.1130/0091-7613(2002)030<0899:BVITOO>2.0.CO;2.

Ishikawa, T., Fujisawa, S., Nagaishi, K., and Masuda, T., 2005, Trace element characteristics of the fluid liberated from amphibolite-facies slab: Inference from the metamorphic sole beneath the Oman ophiolite and implication for boninite genesis: Earth and Planetary Science Letters, v. 240, p. 355–377, https://doi.org/10.1016/j.epsl.2005.09.049.

Ishizuka, O., Tani, K., Reagan, M.K., Kanayama, K., Umino, S., Harigane, Y., Sakamoto, I., Miyajima, Y., Yuasa, M., and Dunkley, D.J., 2011, The timescales of subduction initiation and subsequent evolution of an oceanic island arc: Earth and Planetary Science Letters, v. 306, p. 229–240, https://doi.org/10.1016/j.epsl.2011.04.006.

Jenner, F.E., and O'Neill, H.S.C., 2012, Analysis of 60 elements in 616 ocean floor basaltic glasses: Geochemistry Geophysics Geosystems, v. 13, https://doi.org/10.1029/2011GC004009.

Jochum, K.P., Nohl, U., Herwig, K., Lammel, E., Stoll, B., and Hofmann, A.W., 2005, GeoReM: A new geochemical database for reference materials and isotopic standards: Geostandards and Geoanalytical Research, v. 29, p. 333–338, https://doi.org/10.1111/j.1751-908X.2005.tb00904.x.

Kane, J.S., Potts, P.J., Meisel, T., and Wiedenbeck, M., 2007, International association of geoanalysts' protocol for the certification of geological and environmental reference materials: A supplement: Geostandards and Geoanalytical Research, v. 31, p. 285–288, https://doi.org/10.1111/j.1751-908X.2007.00869.x.

Karsten, J.L., Klein, E.M., and Sherman, S.B., 1996, Subduction zone geochemical characteristics in ocean ridge basalts from the southern Chile Ridge: Implications of modern ridge subduction systems for the Archean: Lithos, v. 37, p. 143–161, https://doi.org/10.1016/0024-4937(95)00034-8.

Kelley, K.A., and Cottrell, E., 2009, Water and the oxidation state of subduction zone magmas: Science, v. 325, p. 605–607, https://doi.org/10.1126/science.1174156.

Klein, E.M., and Langmuir, C.H., 1987, Global correlations of ocean ridge basalt chemistry with axial depth and crustal thickness: Journal of Geophysical Research, Solid Earth, v. 92, p. 8089–8115, https://doi.org/10.1029/JB092iB08p08089.

Koepke, J., Schoenborn, S., Oelze, M., Wittmann, H., Feig, S.T., Hellebrand, E., Boudier, F., and Schoenberg, R., 2009, Petrogenesis of crustal wehrlites in the Oman ophiolite: Experiments and natural rocks: Geochemistry Geophysics Geosystems, v. 10, https://doi.org/10.1029/2009GC002488.

Koga, K.T., Kelemen, P.B., and Shimizu, N., 2001, Petrogenesis of the crust-mantle transition zone and the origin of lower crustal wehrlite in the Oman ophiolite: Geochemistry Geophysics Geosystems, v. 2, https://doi.org/10.1029/2000GC000132.

Kusano, Y., Adachi, Y., Miyashita, S., and Umino, S., 2012, Lava accretion system around mid-ocean ridges: Volcanic stratigraphy in the Wadi Fizh area, northern Oman ophiolite: Geochemistry Geophysics Geosystems, v. 13, https://doi.org/10.1029/2011GC004006.

Kusano, Y., Hayashi, M., Adachi, Y., Umino, S., and Miyashita, S., 2014, Evolution of volcanism and magmatism during initial arc stage: constraints on the tectonic setting of the Oman Ophiolite, *in* Rollinson, H.R., Searle, M.P., Abbasi, I.A., Al-Lazki, A.I., and Al Kindi, M.H., eds., Tectonic Evolution of the Oman Mountains: Geological Society of London Special Publication 392, p. 177–193, https://doi.org/10.1144/SP392.9.

Kusano, Y., Umino, S., Shinjo, R., Ikei, A., Adachi, Y., Miyashita, S., and Arai, S., 2017, Contribution of slab-derived fluid and sedimentary melt in the incipient arc magmas with development of the paleo-arc in the Oman Ophiolite: Chemical Geology, v. 449, p. 206–225, https://doi.org/10.1016/j.chemgeo.2016.12.012.

Lippard, S.J., Shelton, A.W., and Gass, I.G., 1986, The Ophiolite of Northern Oman: Blackwell Scientific Publications Ltd., Geological Society of London Memoir 11, 178 p.

MacLeod, C.J., Lissenberg, J.C., and Bibby, L.E., 2013, "Moist MORB" axial magmatism in the Oman ophiolite: The evidence against a mid-ocean ridge origin: Geology, v. 41, p. 459–462, https://doi.org/10.1130/G33904.1.

Mallmann, G., and O'Neill, H.S.C., 2009, The crystal/melt partitioning of V during mantle melting as a function of oxygen fugacity compared with some other elements (Al, P, Ca, Sc, Ti, Cr, Fe, Ga, Y, Zr and Nb): Journal of Petrology, v. 50, p. 1765–1794, https://doi.org/10.1093/petrology/egp053.

Metcalf, R.V., and Shervais, J.W., 2008, Suprasubduction-zone ophiolites: Is there really an ophiolite conundrum? *in* Wright, J.E., and Shervais, J.W., eds., Ophiolites, Arcs, and Batholiths: A Tribute to Cliff Hopson: Geological Society of America Special Paper 438, p. 191–222, https://doi.org/10.1130/2008.2438(07).

Miyashita, S., Adachi, Y., and Umino, S., 2003, Along-axis magmatic system in the northern Oman ophiolite: Implications of compositional variation of the sheeted dike complex: Geochemistry Geophysics Geosystems, v. 4, https://doi.org/10.1029/2001GC000235.

Moores, E.M., Kellogg, L.H., and Dilek, Y., 2000, Tethyan ophiolites, mantle convection, and tectonic "historical contingency": A resolution of the "ophiolite conundrum," *in* Dilek, Y., Moores, E.M., Elthon, D., and Nicolas, A. eds., Ophiolites and Oceanic Crust: New Insights from Field Studies and the Ocean Drilling Program, Geological Society of America Special Paper 349, p. 3–12, https://doi.org/10.1130/0-8137-2349-3.3.

Nicolas, A., and Boudier, F., 2017, Emplacement of Semail–Emirates ophiolite at ridge–trench collision: Terra Nova, v. 29, p. 127–134, https://doi.org/10.1111/ter.12256.

Nicolas, A., Boudier, F., Ildefonse, B., and Ball, E., 2000, Accretion of Oman and United Arab Emirates ophiolite—Discussion of a new structural map: Marine Geophysical Researches, v. 21, p. 147–180, https://doi.org/10.1023/A:1026769727917.

Pearce, J.A., 1980, Geochemical evidence for the genesis and eruptive setting of lavas from Tethyan ophiolites, *in* Proceedings of the International Ophiolite Symposium, Cyprus 1979, Cyprus, Ministry of Agriculture and Natural Resources, p. 261–272.

Pearce, J.A., 2008, Geochemical fingerprinting of oceanic basalts with applications to ophiolite classification and the search for Archean oceanic crust: Lithos, v. 100, p. 14–48, https://doi.org/10.1016/j.lithos.2007.06.016.

Pearce, J.A., 2014, Immobile element fingerprinting of ophiolites: Elements, v. 10, p. 101–108, http://elements.geoscienceworld.org/content/10/2/101.abstract.

Pearce, J.A., Alabaster, T., Shelton, A.W., and Searle, M.P., 1981, The Oman ophiolite as a Cretaceous arc-basin complex: Evidence and implications: Philosophical Transactions of the Royal Society A, Mathematical, Physical, and Engineering Sciences, v. 300, p. 299–317, https://doi.org/10.1098/rsta.1981.0066.

Pearce, J.A., Lippard, S.J., and Roberts, S., 1984, Characteristics and tectonic significance of supra-subduction zone ophiolites, *in* Kokelaar, B.P., and Howells, M.F., eds., Marginal Basin Geology: Volcanic and Associated Sedimentary and Tectonic Processes in Modern and Ancient Marginal Basins: Geological Society of London Special Publication 16, p. 77–94, https://doi.org/10.1144/GSL.SP.1984.016.01.06.

Peters, D., and Pettke, T., 2016, Evaluation of major to ultra trace element bulk rock chemical analysis of nanoparticulate pressed powder pellets by LA-ICP-MS: Geostandards and Geoanalytical Research, https://doi.org/10.1111/ggr.12125.

Pettke, T., Oberli, F., Audétat, A., Guillong, M., Simon, A.C., Hanley, J.J., and Klemm, L.M., 2012, Recent developments in element concentration and isotope ratio analysis of individual fluid inclusions by laser ablation single and multiple collector ICP-MS: Ore Geology Reviews, v. 44, p. 10–38, https://doi.org/10.1016/j.oregeorev.2011.11.001.

Reagan, M.K., Ishizuka, O., Stern, R.J., Kelley, K.A., Ohara, Y., Blichert-Toft, J., Bloomer, S.H., Cash, J., Fryer, P., Hanan, B.B., Hickey-Vargas, R., Ishii, T., Kimura, J.I., Peate, D.W., et al., 2010, Fore-arc basalts and subduction initiation in the Izu-Bonin-Mariana system: Geochemistry Geophysics Geosystems, v. 11, https://doi.org/10.1029/2009GC002871.

Reagan, M.K., McClelland, W.C., Girard, G., Goff, K.R., Peate, D.W., Ohara, Y., and Stern, R.J., 2013, The geology of the southern Mariana fore-arc crust: Implications for the scale of Eocene volcanism in the western Pacific: Earth and Planetary Science Letters, v. 380, p. 41–51, https://doi.org/10.1016/j.epsl.2013.08.013.

Reagan, M.K., Heaton, D.E., Schmitz, M.D., Pearce, J.A., Shervais, J.W., and Koppers, A.A.P., 2019, Forearc ages reveal extensive short-lived and rapid seafloor spreading following subduction initiation: Earth and Planetary Science Letters, v. 506, p. 520–529, https://doi.org/10.1016/j.epsl.2018.11.020.

Regelous, M., Haase, K.M., Freund, S., Keith, M., Weinzierl, C.G., Beier, C., Brandl, P.A., Endres, T., and Schmidt, H., 2014, Formation of the Troodos Ophiolite at a triple junction: Evidence from trace elements in volcanic glass: Chemical Geology, v. 386, p. 66–79, https://doi.org/10.1016/j.chemgeo.2014.08.006.

Resing, J.A., Rubin, K.H., Embley, R.W., Lupton, J.E., Baker, E.T., Dziak, R.P., Baumberger, T., Lilley, M.D., Huber, J.A., Shank, T.M., Butterfield, D.A., Clague, D.A., Keller, N.S., Merle, S.G., et al., 2011, Active submarine eruption of boninite in the northeastern Lau Basin: Nature Geoscience, v. 4, p. 799, https://doi.org/10.1038/ngeo1275.

Rioux, M., Bowring, S., Kelemen, P., Gordon, S., Miller, R., and Dudás, F., 2013, Tectonic development of the Samail ophiolite: High-precision U-Pb zircon geochronology and Sm-Nd isotopic constraints on crustal growth and emplacement: Journal of Geophysical Research. Solid Earth, v. 118, p. 2085–2101, https://doi.org/10.1002/jgrb.50139.

Rioux, M., Garber, J., Bauer, A., Bowring, S., Searle, M., Kelemen, P., and Hacker, B., 2016, Synchronous formation of the metamorphic sole and igneous crust of the Semail ophiolite: New constraints on the tectonic evolution during ophiolite formation from high-precision U–Pb zircon geochronology: Earth and Planetary Science Letters, v. 451, p. 185–195, https://doi.org/10.1016/j.epsl.2016.06.051.

Rollinson, H., 2015, Slab and sediment melting during subduction initiation: granitoid dykes from the mantle section of the Oman ophiolite: Contributions to Mineralogy and Petrology, v. 170, https://doi.org/10.1007/s00410-015-1177-9.

Rollinson, H., and Adetunji, J., 2013, Mantle podiform chromitites do not form beneath mid-ocean ridges: A case study from the Moho transition zone of the Oman ophiolite: Lithos, v. 177, p. 314–327, https://doi.org/10.1016/j.lithos.2013.07.004.

Rollinson, H., and Adetunji, J., 2015, The geochemistry and oxidation state of podiform chromitites from the mantle section of the Oman ophiolite: A review: Gondwana Research, v. 27, p. 543–554, https://doi.org/10.1016/j.gr.2013.07.013.

Rospabé, M., Ceuleneer, G., Benoit, M., Abily, B., and Pinet, P., 2017, Origin of the dunitic mantle-crust transition zone in the Oman ophiolite: The interplay between percolating magmas and high-temperature hydrous fluids: Geology, v. 45, p. 471–474, https://doi.org/10.1130/G38778.1.

Shervais, J.W., 1982, TiV plots and the petrogenesis of modern and ophiolitic lavas: Earth and Planetary Science Letters, v. 59, p. 101–118, https://doi.org/10.1016/0012-821X(82)90120-0.

Shervais, J.W., Reagan, M., Haugen, E., Almeev, R., Pearce, J., Prytulak, J., Ryan, J.G., Whattam, S., Godard, M., Chapman, T., Li, H., Kurz, W., Nelson, W.R., Heaton, D., et al., 2018, Magmatic Response to Subduction Initiation, Part I: Forearc basalts of the Izu-Bonin Arc from IODP Expedition 352: Geochemistry Geophysics Geosystems, v. 20, p. 314–338, https://doi.org/10.1029/2018GC007731.

Spencer, C.J., Cavosie, A.J., Raub, T.D., Rollinson, H., Jeon, H., Searle, M.P., Miller, J.A., McDonald, B.J., and Evans, N.J., 2017, Evidence for melting mud in Earth's mantle from extreme oxygen isotope signatures in zircon: Geology, v. 45, p. 975–978, https://doi.org/10.1130/G39402.1.

Stern, R.J., Reagan, M., Ishizuka, O., Ohara, Y., and Whattam, S., 2012, To understand subduction initiation, study forearc crust: To understand forearc crust, study ophiolites: Lithosphere, v. 4, p. 469–483, https://doi.org/10.1130/L183.1.

Sturm, M.E., Klein, E.M., Karsten, J.L., and Karson, J.A., 2000, Evidence for subduction-related contamination of the mantle beneath the southern Chile Ridge; implications for ambiguous ophiolite compositions, *in* Dilek, Y., Moores, E.M., Elthon, D., and Nicolas, A., eds., Ophiolites and Oceanic Crust; New Insights from Field Studies and the Ocean Drilling Program: Geological Society of America Special Paper 349, p. 13–20, https://doi.org/10.1130/0-8137-2349-3.13.

Umino, S., Yanai, S., Jaman, A.R., Nakamura, Y., and Iiyama, J.T., 1990, The transition from spreading to subduction: evidence from the Semail ophiolite, northern Oman mountains, *in* Ophiolites, Oceanic Crustal Analogues, Proceedings of the Symposium "Troodos 1987": Nicosia, Cyprus Geological Survey Department, p. 375–385

Whattam, S.A., and Stern, R.J., 2011, The "subduction initiation rule": A key for linking ophiolites, intra-oceanic forearcs, and subduction initiation: Contributions to Mineralogy and Petrology, v. 162, p. 1031–1045, https://doi.org/10.1007/s00410-011-0638-z.

Woelki, D., Regelous, M., Haase, K.M., Romer, R.H.W., and Beier, C., 2018, Petrogenesis of boninitic lavas from the Troodos Ophiolite, and comparison with Izu–Bonin–Mariana fore-arc crust: Earth and Planetary Science Letters, https://doi.org/10.1016/j.epsl.2018.06.041.

Workman, R.K., and Hart, S.R., 2005, Major and trace element composition of the depleted MORB mantle (DMM): Earth and Planetary Science Letters, v. 231, p. 53–72, https://doi.org/10.1016/j.epsl.2004.12.005.

Yogodzinski, G.M., Bizimis, M., Hickey-Vargas, R., McCarthy, A., Hocking, B.D., Savov, I.P., Ishizuka, O., and Arculus, R., 2018, Implications of Eocene-age Philippine Sea and forearc basalts for initiation and early history of the Izu-Bonin-Mariana arc: Geochimica et Cosmochimica Acta, v. 228, p. 136–156, https://doi.org/10.1016/j.gca.2018.02.047.

MANUSCRIPT RECEIVED 15 OCTOBER 2018
REVISED MANUSCRIPT RECEIVED 28 JANUARY 2019
MANUSCRIPT ACCEPTED 22 FEBRUARY 2019